Numerical modeling of transient two-dimensional viscoelastic waves

Bruno Lombard, Joël Piraux

Numerical modeling of transient two-dimensional viscoelastic waves

Bruno Lombard[a,*], Joël Piraux[a]

[a] *Laboratoire de Mécanique et d'Acoustique, 13402, Marseille, France*

Abstract

This paper deals with the numerical modeling of transient mechanical waves in linear viscoelastic solids. Dissipation mechanisms are described using the Zener model. No time convolutions are required thanks to the introduction of memory variables that satisfy local-in-time differential equations. By appropriately choosing the Zener parameters, it is possible to accurately describe a large range of materials, such as solids with constant quality factors. The evolution equations satisfied by the velocity, the stress, and the memory variables are written in the form of a first-order system of PDEs with a source term. This system is solved by splitting it into two parts: the propagative part is discretized explicitly, using a fourth-order ADER scheme on a Cartesian grid, and the diffusive part is then solved exactly. Jump conditions along the interfaces are discretized by applying an immersed interface method. Numerical experiments of wave propagation in viscoelastic and fluid media show the efficiency of this numerical modeling for dealing with challenging problems, such as multiple scattering configurations.

Keywords: wave propagation, Zener model, memory variables, ADER schemes, Cartesian grid methods, immersed interface method
2000 MSC: 35L50, 65M06
PACS: 43.20.-Gp, 46.35.+z, 46.40.-f

*Corresponding author. Tel.: +33 491 16 44 13.
Email addresses: lombard@lma.cnrs-mrs.fr (Bruno Lombard), piraux@lma.cnrs-mrs.fr (Joël Piraux)

1. Introduction

Wave motion in real media differs in many aspects from motion in an idealized elastic medium. The dispersion and attenuation induced, for instance, by grain-to-grain friction can greatly affect the amplitude of the waves and their arrival times. In the case of small perturbations, linear models of viscoelasticity provide reasonably accurate means of describing these effects. Viscoelastic constitutive laws give the stress in terms of the past strain rate history.

The aim of this paper is to simulate the propagation and the diffraction of transient viscoelastic waves. We propose a new approach in three steps:

(i) The Zener model is used [8]. The convolution products are then replaced by a set of local-in-time differential equations coupled with the evolution equations of velocity and stress. Moreover, usual attenuation laws can be approximated closely.

(ii) The evolution equations are splitted into two parts: a propagative part, which is solved using a fourth-order finite-difference ADER scheme on a Cartesian grid [29]; and a diffusive part, which is solved analytically. Doing so ensures an optimal condition of stability.

(iii) The jump conditions along the interfaces are discretized by an immersed interface method, which introduces a subcell resolution of the geometry and maintains the convergence rate of the scheme despite the non-smoothness of the solution. See [19] for an overview of these methods.

The model of Zener (i) has been addressed by various means, such as finite difference methods [28, 31], spectral methods [7], spectral-element methods [16], finite element methods [14, 3], to cite only a few. The steps (ii) and (iii) combine the computational efficiency of Cartesian grid methods and an accurate description of the interfaces, as stated in the case of non-dissipative media [22, 23] and applied to computationally challenging configurations [9].

The article is organized as follows. In section 2, the Zener model is presented; the method used to determine its parameters to simulate a given quality factor is also described. In section 3, the evolution equations are written in the form of a first-order hyperbolic system with a source term; the jump conditions along the interfaces are also stated. The numerical methods used are introduced in section 4, including the numerical scheme and the splitting for the integration of the evolution equations, and the immersed

interface method for the discretization of the jump conditions. Numerical experiments are presented in section 5 in the case of a viscoelastic / fluid interface. Comparisons with analytical solutions are made in some academic cases. A numerical experiment involving multiple scattering in a random medium also confirms the efficiency of the approach. Lastly, the perspectives are discussed in section 6.

2. Physical modeling

2.1. Constitutive law

In a viscoelastic solid undergoing small perturbations, the stress depends linearly on the history of the past strain rates. In 1D, one writes

$$\sigma = \psi * \frac{\partial \varepsilon}{\partial t}, \tag{1}$$

where σ is the stress, $\varepsilon = \frac{\partial u}{\partial x}$ is the strain, u is the displacement, $\psi(t)$ is the relaxation function, and $*$ denotes the time convolution. The *Zener model* for viscoelasticity chosen here accurately mimics the mechanical behavior of classical viscoelastic media during relaxation experiments:

$$\psi(t) = \pi_r \left(1 + \sum_{\ell=1}^{N} \kappa_\ell \, e^{-\theta_\ell \, t} \right) H(t), \tag{2}$$

where H refers to the Heaviside distribution, N is the number of relaxation mechanisms, θ_ℓ are relaxation frequencies, and the coefficients κ_ℓ are strictly positive. The instantaneous unrelaxed state is denoted by π_u, and at the end of the process, the relaxation function has returned completely to the positive relaxed modulus π_r, where $0 < \pi_r < \pi_u$. The phase velocity of the waves propagating in a Zener material increases with the frequency, from $c_0 = \sqrt{\pi_r/\rho}$ at null frequency to $c_\infty = \sqrt{\pi_u/\rho}$ at infinite frequency, where ρ is the density [8].

2.2. Determination of the parameters

Let $\mathcal{F}$ be the Fourier transform of a function $g(t)$

$$\mathcal{F}\,(g) = \int_{-\infty}^{+\infty} g(t) \, e^{-i\,\omega\,t} \, dt, \tag{3}$$

where ω is the angular frequency. From (2), the modulus of viscoelasticity $M(\omega) = \mathcal{F}(\frac{\partial \psi}{\partial t})$ is:

$$M(\omega) = \pi_r \left(1 + i\,\omega \sum_{\ell=1}^{N} \frac{\kappa_\ell}{\theta_\ell + i\,\omega} \right), \tag{4}$$

and the ratio between the imaginary and real parts of M is:

$$Q^{-1}(\omega) = \frac{\displaystyle\sum_{\ell=1}^{N} \frac{\omega\,\theta_\ell\,\kappa_\ell}{\theta_\ell^2 + \omega^2}}{\displaystyle 1 + \sum_{\ell=1}^{N} \frac{\omega^2\,\kappa_\ell}{\theta_\ell^2 + \omega^2}}. \tag{5}$$

The quality factor Q characterizes the attenuation of the viscoelastic waves.

To determine the $2\,N$ coefficients κ_ℓ and θ_ℓ in (2), we choose to minimize the distance between $Q^{-1}(\omega)$ and a given $Q_{ref}^{-1}(\omega)$ in a band of angular frequencies $[\omega_0,\, \omega_1]$. Here we have implemented a classical linear least-squares minimization procedure in the L_2 norm [12, 13, 4]. Relaxation frequencies are distributed linearly on a logarithmic scale of N points, ranging from $f_0 = \omega_0 \,/\, (2\,\pi)$ to $f_1 = \omega_1 \,/\, (2\,\pi)$ [14]

$$\theta_\ell = \frac{\omega_0}{2\,\pi} \left(\frac{\omega_1}{\omega_0} \right)^{\frac{\ell-1}{N-1}}, \qquad \ell = 1, ..., N. \tag{6}$$

The angular frequencies ω_0 and ω_1 obviously depend on the spectra of the source. The coefficients κ_ℓ are then obtained by solving the over-determined linear system deduced from (5)

$$\sum_{\ell=1}^{N} \frac{\tilde{\omega}_k \,\left(\theta_\ell - \tilde{\omega}_k\, Q_{ref}^{-1}(\tilde{\omega}_k)\right)}{\theta_\ell^2 + \tilde{\omega}_k^2}\, \kappa_\ell = Q_{ref}^{-1}(\tilde{\omega}_k), \qquad k = 1, ..., 2\,N - 1, \tag{7}$$

where $\tilde{\omega}_k$ are distributed linearly on a logarithmic scale of $2\,N - 1$ points

$$\tilde{\omega}_k = \omega_0 \left(\frac{\omega_1}{\omega_0} \right)^{\frac{k-1}{2\,(N-1)}}, \qquad k = 1, ..., 2\,N - 1. \tag{8}$$

In our numerical experiments, calculations based on (7) have never yielded non-physical negative values of κ_ℓ, even with highly attenuating media (typically $Q_{ref} = 5$). If necessary, more sophisticated methods can be applied.

For instance, a nonlinear least-squares constraint optimization was used in [3] to ensure that the coefficients κ_ℓ were positive. An alternative method of optimization in the norm L_∞ was presented in [2], but this latter method is restricted to materials with constant Q_{ref}.

To determine the number of relaxation mechanisms N, one can compare Q_{ref} and the quality factor Q deduced from (5) after optimization. However, the modeling error in the time domain is not easily deduced. A second idea consists in comparing the transient 1-D analytical solutions associated with Q_{ref} and Q. These solutions are calculated using classical Fourier techniques, which are not described here.

2.3. Numerical examples

The determination of the parameters in (2) is illustrated in figure 1. The set up is the same here as in section 5: the source is a smoothly truncated sinusoid of central frequency $f_c = 50$ Hz; the optimization of the quality factor is done between $f_0 = f_c \,/\, 10$ and $f_1 = 10\, f_c$; the physical parameters are $\rho = 1200$ kg/m^3, $c_0 = 2800$ m/s, $Q_{ref} = 20$. Considering a constant Q_{ref} is usual in geosciences, where the real media show a quasi-constant quality factor within very wide frequency ranges [1]. In addition, the exact solution associated with a constant Q_{ref} is particularly simple to obtain, involving the Kjartansson formula [17]. Note that non-constant Q_{ref} can also be considered in numerical modeling without any restrictions.

Figure 1 compares the quality factor (a) and the time-domain exact solutions (b), when $N = 1$ or $N = 3$. Increasing N clearly decreases the error introduced by describing the constant quality factor medium in terms of a finite number of relaxation mechanisms. At the same time and as seen in section 3.2, increasing N greatly increases the computational cost, especially the memory requirements. In practice, $N > 3$ is rarely implemented in the literature, and $N = 1$ is widely used, especially in the 3-D context [28].

Dispersion and relaxation curves shown in figure 1 (c) and (d) are computed taking $N = 3$ relaxation mechanisms. One observes the predicted behavior: strict increase of the phase velocity from c_0 to c_∞ (c), strict decrease of the relaxation function from π_u to π_r (d).

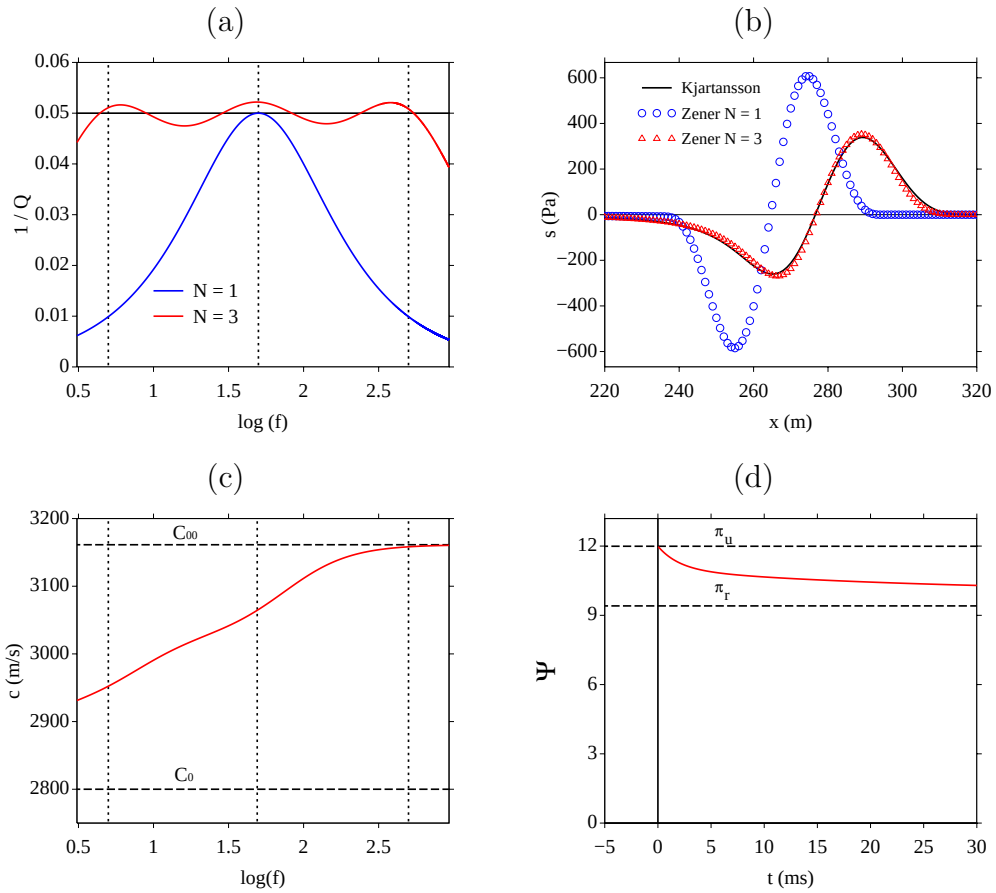

Figure 1: Determination of Zener parameters, with $Q_{ref} = 20$, $f_c = 50$ Hz, and $N = 1$ or $N = 3$ relaxation mechanisms. Quality factors (a); the solid horizontal line gives the exact value $1 \,/\, Q_{ref}$. Time-domain 1-D analytical solutions obtained with the constant-Q model (Kjartansson's model) and the Zener model (b). Phase velocity (c) and relaxation function (d) obtained with $N = 3$. Physical parameters are those used in section 5. In (a) and (c), the dotted vertical lines give the relaxation frequencies when $N = 3$.

3. Initial boundary-value problem

3.1. Constitutive law in two-dimensions

The viscoelastic law (1) is generalized so that it applies to all space dimensions. In the 2-D case, the constitutive law governing a linear isotropic viscoelastic medium is [8]

$$\sigma_{ij} = (\psi_\pi(t) - 2\,\psi_\mu(t)) * \frac{\partial\,\varepsilon_{kk}}{\partial\,t}\,\delta_{ij} + 2\,\psi_\mu(t) * \frac{\partial\,\varepsilon_{ij}}{\partial\,t}, \tag{9}$$

where σ_{ij} and ε_{ij} are the components of the stress and strain tensors, and δ_{ij} is the Kronecker symbol. With the Zener model, the relaxation functions ψ_π and ψ_μ are given by

$$\begin{aligned} \psi_\pi(t) &= \pi_r \left(1 + \sum_{\ell=1}^{N} \kappa_\ell^p\, e^{-\theta_\ell\, t} \right) H(t), \\ \psi_\mu(t) &= \mu_r \left(1 + \sum_{\ell=1}^{N} \kappa_\ell^s\, e^{-\theta_\ell\, t} \right) H(t), \end{aligned} \tag{10}$$

where $\pi_r = \rho\, c_{p_0}^2$ and $\mu_r = \rho\, c_{s_0}^2$ are relaxed moduli under compressional and shear loads. The phase velocities of the compressional (P) and shear (S) waves at zero frequency are denoted c_{p0} and c_{s0}. The unrelaxed moduli are written

$$\pi_u = \pi_r \left(1 + \sum_{\ell=1}^{N} \kappa_\ell^p \right) = \rho\, c_{p_\infty}^2, \qquad \mu_u = \mu_r \left(1 + \sum_{\ell=1}^{N} \kappa_\ell^s \right) = \rho\, c_{s_\infty}^2, \tag{11}$$

where c_{p_∞} and c_{s_∞} are the phase velocities of P and S waves at infinite frequency. The parameters θ_ℓ, κ_ℓ^p and κ_ℓ^s in (10) are determined as in section 2.1 from the quality factors Q_{ref}^p and Q_{ref}^s of P and S waves. Usually, $Q_{ref}^s < Q_{ref}^p$: the S waves are more attenuated than the P waves. The relaxation frequencies θ_ℓ are the same with both P and S waves, since they depend only on the frequency band of interest (6). In addition, describing P and S waves with identical relaxation times, as well as identical numbers of relaxation mechanisms, greatly reduces the memory requirements [28, 31].

3.2. Evolution equations

To obtain the evolution equations satisfied by σ_{ij}, the constitutive law (9) is differentiated in terms of t, taking (10). If $i = j$, we obtain

$$\frac{\partial \sigma_{ij}}{\partial t} = (\pi_u - 2\,\mu_u)\,\frac{\partial v_k}{\partial x_k} + 2\,\mu_u\,\frac{\partial v_i}{\partial x_j} + \sum_{\ell=1}^{N} \xi_{ij\ell}, \tag{12}$$

where the $\xi_{ij\ell}$ are called *memory variables*

$$\xi_{ij\ell} = -\theta_\ell\,(\pi_r\,\kappa_\ell^p - 2\,\mu_r\,\kappa_\ell^s)\,e^{-\theta_\ell\,t}H(t) * \frac{\partial v_k}{\partial x_k} - 2\,\mu_r\,\theta_\ell\,\kappa_\ell^s\,e^{-\theta_\ell\,t}H(t) * \frac{\partial v_i}{\partial x_j}. \tag{13}$$

These memory variables satisfy the differential equations

$$\frac{d\,\xi_{ij\ell}}{d\,t} = -\theta_\ell\,\left(\xi_{ij\ell} + (\pi_r\,\kappa_\ell^p - 2\,\mu_r\,\kappa_\ell^s)\,\frac{\partial v_k}{\partial x_k} + 2\,\mu_r\,\kappa_\ell^s\,\frac{\partial v_i}{\partial x_j}\right), \qquad \ell = 1, ..., N. \tag{14}$$

In the same way, if $i \neq j$, we obtain

$$\frac{\partial \sigma_{ij}}{\partial t} = \mu_u\left(\frac{\partial v_i}{\partial x_j} + \frac{\partial v_j}{\partial x_i}\right) + \sum_{\ell=1}^{N} \xi_{ij\ell}, \tag{15}$$

with the memory variables

$$\xi_{ij\ell} = -\mu_r\,\theta_\ell\,\kappa_\ell^s\,e^{-\theta_\ell\,t}H(t) * \left(\frac{\partial v_i}{\partial x_j} + \frac{\partial v_j}{\partial x_i}\right), \tag{16}$$

that satisfy the differential equations

$$\frac{d\,\xi_{ij\ell}}{d\,t} = -\theta_\ell\,\left(\xi_{ij\ell} + \mu_r\,\kappa_\ell^s\,\left(\frac{\partial v_i}{\partial x_j} + \frac{\partial v_j}{\partial x_i}\right)\right), \qquad \ell = 1, ..., N. \tag{17}$$

The convolutions in (13) and (16) induced by the convolution in (9) are no longer involved in (14) and (17): adding a set of memory variables that satisfy local-in-time differential equations avoids to store the past values of the solution. In 2-D contexts, combining (12), (14), (15) and (17) with

Newton's law yields a system of $5+3\,N$ partial differential equations

$$\left\{\begin{array}{l}
\dfrac{\partial\, v_1}{\partial\, t}-\dfrac{1}{\rho}\left(\dfrac{\partial\,\sigma_{11}}{\partial\, x}+\dfrac{\partial\,\sigma_{12}}{\partial\, y}\right)=0,\\
\dfrac{\partial\, v_2}{\partial\, t}-\dfrac{1}{\rho}\left(\dfrac{\partial\,\sigma_{12}}{\partial\, x}+\dfrac{\partial\,\sigma_{22}}{\partial\, y}\right)=0,\\
\dfrac{\partial\,\sigma_{11}}{\partial\, t}-\pi_u\,\dfrac{\partial\, v_1}{\partial\, x}-(\pi_u-2\,\mu_u)\,\dfrac{\partial\, v_2}{\partial\, y}=\displaystyle\sum_{\ell=1}^{N}\xi_{11\ell},\\
\dfrac{\partial\,\sigma_{12}}{\partial\, t}-\mu_u\left(\dfrac{\partial\, v_1}{\partial\, y}+\dfrac{\partial\, v_2}{\partial\, x}\right)=\displaystyle\sum_{\ell=1}^{N}\xi_{12\ell},\\
\dfrac{\partial\,\sigma_{22}}{\partial\, t}-(\pi_u-2\,\mu_u)\,\dfrac{\partial\, v_1}{\partial\, x}-\pi_u\,\dfrac{\partial\, v_2}{\partial\, y}=\displaystyle\sum_{\ell=1}^{N}\xi_{22\ell},\\
\dfrac{\partial\,\xi_{11\ell}}{\partial\, t}+\theta_\ell\,\left(\pi_r\,\kappa_\ell^p\dfrac{\partial\, v_1}{\partial\, x}+(\pi_r\,\kappa_\ell^p-2\,\mu_r\,\kappa_\ell^s)\,\dfrac{\partial\, v_2}{\partial\, y}\right)=-\theta_\ell\,\xi_{11\ell},\quad \ell=1,...,\,N\\
\dfrac{\partial\,\xi_{12\ell}}{\partial\, t}+\mu_r\,\theta_\ell\,\kappa_\ell^s\,\left(\dfrac{\partial\, v_1}{\partial\, y}+\dfrac{\partial\, v_2}{\partial\, x}\right)=-\theta_\ell\,\xi_{12\ell},\quad \ell=1,...,\,N\\
\dfrac{\partial\,\xi_{22\ell}}{\partial\, t}+\theta_\ell\,\left((\pi_r\,\kappa_\ell^p-2\,\mu_r\,\kappa_\ell^s)\,\dfrac{\partial\, v_1}{\partial\, x}+\pi_r\,\kappa_\ell^p\,\dfrac{\partial\, v_2}{\partial\, y}\right)=-\theta_\ell\,\xi_{22\ell},\quad \ell=1,...,\,N.
\end{array}\right. \tag{18}$$

Setting

$$\mathbf{U}=(v_1,\,v_2,\,\sigma_{11},\,\sigma_{12},\,\sigma_{22},\,\xi_{111},...,\,\xi_{11N},\,\xi_{121},...,\,\xi_{12N},\,\xi_{221},...\,\xi_{22N})^T\,, \tag{19}$$

one can write (18) in the form of a first-order linear system with a source term

$$\frac{\partial}{\partial\, t}\,\mathbf{U}+\mathbf{A}\,\frac{\partial}{\partial\, x}\,\mathbf{U}+\mathbf{B}\,\frac{\partial}{\partial\, y}\,\mathbf{U}=-\mathbf{S}\,\mathbf{U}, \tag{20}$$

where $\mathbf{A}$, $\mathbf{B}$ and $\mathbf{S}$ are $(5+3\,N)\times(5+3\,N)$ matrices. The eigenvalues of $\mathbf{A}$ and $\mathbf{B}$ are real: $\pm c_{p\infty}$, $\pm c_{s\infty}$, and 0 with multiplicity $3\,N+1$. As deduced from (6), the spectral radius of $\mathbf{S}$ is

$$R(\mathbf{S})=\theta_N=\frac{\omega_1}{2\,\pi}=f_1. \tag{21}$$

For further use, we introduce the restriction of $\mathbf{U}$ to the velocity and stress components and without any memory variables:

$$\overline{\mathbf{U}}=(v_1,\,v_2,\,\sigma_{11},\,\sigma_{12},\,\sigma_{22})^T\,. \tag{22}$$

An overline is also used to denote the restricted 5×5 matrices $\overline{\mathbf{A}}$ and $\overline{\mathbf{B}}$ involving only the velocity and stress components.

Even in non-viscoelastic subdomains, the evolution equations are written in the same way as (20). For instance, Ω_1 is assumed to be a fluid medium in section 3.3 and in the numerical experiments. In this case, $\mathbf{U} = \overline{\mathbf{U}} = (v_1, v_2, p)^T$, where p is the acoustic pressure, $\mathbf{A}$ and $\mathbf{B}$ are 3×3 matrices, and $\mathbf{S} = \mathbf{0}$. Lastly, subscripts will be used to denote the medium under investigation: as an example, $\mathbf{A}_0$ is the matrix $\mathbf{A}$ in Ω_0.

3.3. Interface conditions

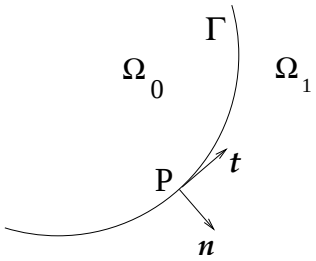

Figure 2: Interface Γ between two media Ω_0 et Ω_1.

The physical parameters defined in section 3.2 can vary discontinuously across interfaces. In what follows, we will focus on two domains Ω_0 and Ω_1, which are separated by a stationary interface Γ described by a parametric equation $(x(\tau), y(\tau))$ (figure 2). The domain Ω_0 contains a viscoelastic medium described by Zener's model: the constitutive law and the evolution equations in Ω_0 are described in sections 2.1 and 3.2. The domain Ω_1 can contain vacuum, a perfect fluid, an elastic solid or any other viscoelastic medium: all these combinations have been implemented numerically and tested. In the rest of the study, we will focus on the case where Ω_1 contains a fluid. In this case, the interface conditions are

$$[\mathbf{v}.\mathbf{n}] = 0, \qquad (\sigma.\mathbf{n}).\mathbf{n} = -p.\mathbf{n}^2, \qquad (\sigma.\mathbf{n}).\mathbf{t} = 0, \tag{23}$$

where [.] refers to the jump from Ω_0 to Ω_1, and the unit tangential vector $\mathbf{t}$ and the unit normal vector $\mathbf{n}$ are

$$\mathbf{t} = \frac{1}{\sqrt{x'^2 + y'^2}} \left(x', \, y'\right)^T, \qquad \mathbf{n} = \frac{1}{\sqrt{x'^2 + y'^2}} \left(y', \, -x'\right)^T. \tag{24}$$

Derivatives $x' = \frac{dx}{d\tau}$ and $y' = \frac{dy}{d\tau}$ are assumed to be continuous everywhere along Γ, and to be differentiable as many times as required.

The system of PDEs (18) does not involve spatial derivatives of $\xi_{ij\ell}$. The memory variables therefore do not satisfy any interface conditions. As a consequence, only the velocity and stress components of $\overline{\mathbf{U}}$ in (22) are considered when dealing with interface conditions. In section 4.2, we will write the interface conditions satisfied by the spatial derivatives of $\overline{\mathbf{U}}$ up to the k-th order, and hence the following notation is introduced:

$$\mathbf{U}_m^k = \lim_{M \to P,\, M \in \Omega_m} \left(\overline{\mathbf{U}}^T, ..., \frac{\partial^\alpha}{\partial\, x^{\alpha-\beta}\, \partial\, y^\beta}\, \overline{\mathbf{U}}^T, ..., \frac{\partial^k}{\partial\, y^k}\, \overline{\mathbf{U}}^T \right)^T, \tag{25}$$

where $\alpha = 0, ..., k$, $\beta = 0, ..., \alpha$, and $m = 0, 1$ denotes the number of the medium Ω_m. The interface conditions of $\overline{\mathbf{U}}$ are then written

$$\begin{aligned} &\mathbf{C}_1^0\, \mathbf{U}_1^0 = \mathbf{C}_0^0\, \mathbf{U}_0^0, \\ &\mathbf{L}_1^0\, \mathbf{U}_1^0 = \mathbf{0}, \qquad \mathbf{L}_0^0\, \mathbf{U}_0^0 = \mathbf{0}, \end{aligned} \tag{26}$$

where $\mathbf{C}_m^0$ are the matrices of the jump conditions, and $\mathbf{L}_m^0$ are the matrices of the boundary conditions. With this formalism, the viscoelastic / fluid interface conditions (23) and the vectors (24) yield

$$\begin{aligned} \mathbf{C}_0^0(\tau) &= \begin{pmatrix} y' & -x' & 0 & 0 & 0 \\ 0 & 0 & y'^2 & -2\, x' y' & x'^2 \end{pmatrix}, \\ \mathbf{C}_1^0(\tau) &= \begin{pmatrix} y' & -x' & 0 \\ 0 & 0 & -\left(x'^2 + y'^2\right) \end{pmatrix}, \\ \mathbf{L}_0^0(\tau) &= \begin{pmatrix} 0 & 0 & x' y' & y'^2 - x'^2 & -x' y' \end{pmatrix}, \quad \mathbf{L}_1^0(\tau) = \begin{pmatrix} 0 & 0 & 0 \end{pmatrix}. \end{aligned} \tag{27}$$

4. Numerical modeling

4.1. Numerical scheme

Let us take a uniform grid, with the spatial mesh size $\Delta\, x = \Delta\, y$ and the time step $\Delta\, t$. An approximation $\mathbf{U}_{i,j}^n$ of $\mathbf{U}(x_i = i\, \Delta\, x,\, y_j = j\, \Delta\, y,\, t_n = n\, \Delta\, t)$ is sought. The numerical methods recalled in section 1 usually consist in simultaneously discretizing the propagating part and the source term in (20).

This approach has two drawbacks. First, building unsplit methods for (18) is a difficult task [18], whereas large classes of methods already exist for hyperbolic systems without the source term $\mathbf{S}\,\mathbf{U}$. Secondly, a Von-Neumann stability analysis typically yields

$$\Delta t \leq \min\left(\frac{\gamma\,\Delta x}{c_{p\infty}},\, \frac{2}{R(\mathbf{S})}\right), \tag{28}$$

where γ depends on the scheme. Based on (21) and (28), the spectral radius of $\mathbf{S}$ induces a more restrictive bound than the classical CFL condition if $f_1 \geq 2\,c_{p_\infty} / (\gamma\,\Delta x)$, where f_1 is the maximum frequency considered during the determination of the parameters (section 2.2). The efficiency of the scheme is therefore penalized if large values of f_1 are taken.

A more efficient approach consists in splitting (18) and alternatively solving the propagative part

$$\frac{\partial}{\partial t}\,\mathbf{U} + \mathbf{A}\,\frac{\partial}{\partial x}\,\mathbf{U} + \mathbf{B}\,\frac{\partial}{\partial y}\,\mathbf{U} = \mathbf{0}, \tag{29}$$

and then the diffusive part

$$\frac{\partial}{\partial t}\,\mathbf{U} = -\mathbf{S}\,\mathbf{U}, \tag{30}$$

with Strang's splitting [18]. During the first of these two stages, the viscoelastic medium behaves like an elastic medium with Lamé coefficients $\lambda = \pi_u - 2\,\mu_u$ and $\mu = \mu_u$. The equation (29) can be solved by applying any explicit two time step spatially-centered flux-conserving scheme for hyperbolic systems, giving $\mathbf{U}_{i,j}^{n+1/2}$. In the numerical experiments performed in section 5, a fourth-order ADER scheme [29] is used, with a centered stencil comprising 25 nodes. On Cartesian grids, this scheme amounts to a fourth-order Lax-Wendroff scheme. It is dispersive of order 4 and dissipative of order 6, with a stability limit $\gamma = 1$ [21]. Other single-grid schemes can be used without any restrictions.

The equation (30) is then solved exactly:

$$\begin{aligned}
v_p^{n+1} &= v_p^{n+1/2}, \\
\sigma_{pq}^{n+1} &= \sigma_{pq}^{n+1/2} + \sum_{\ell=1}^{N} \frac{1}{\theta_\ell}\left(1 - e^{-\theta_\ell\,T}\right)\,\xi_{pq\ell}^{n+1/2}, \\
\xi_{pq\ell}^{n+1} &= e^{-\theta_r\,T}\,\xi_{pq\ell}^{n+1/2}, \quad \ell = 1, ..., N,
\end{aligned} \tag{31}$$

where $(p,\, q) = \{(1,1),\, (1,2),\, (2,2)\}$, $T = \frac{\Delta t}{2}$ at the first and last iterations, and $T = \Delta t$ otherwise [18]. The splitting (29)-(30) and the exact integration (31) yields the optimum CFL stability condition: $\frac{c_{p\infty}\,\Delta t}{\Delta x} \leq \gamma$.

Since the matrices $\mathbf{A}$ and $\mathbf{B}$ do not commute with $\mathbf{S}$, the Strang's splitting decreases the theoretical order of convergence from 4 to 2 [18]. It is nevertheless preferable to use a fourth-order accurate scheme such as ADER 4 rather than a second-order scheme such as the Lax-Wendroff scheme: the stability limit is higher, and the numerical artifacts such as dispersion, attenuation and anisotropy, are much smaller in the case of ADER 4.

4.2. Immersed interface method

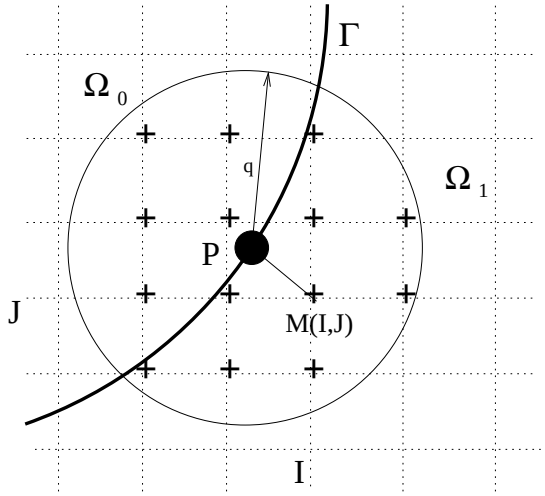

Figure 3: $M(x_I,\, y_J) \in \Omega_1$ is a grid node where a modified value $\mathbf{U}^*_{I,J}$ is computed; P is the orthogonal projection of M onto the interface Γ. The grid nodes used to compute $\mathbf{U}^*_{I,J}$ are inside the circle with radius q and centered on P; they are denoted by $+$.

To solve the propagative part (29) accurately at a grid node, the solution $\mathbf{U}$ has to be sufficiently smooth on the whole stencil around this node. In practice, we can focus on the velocity and stress components in $\overline{\mathbf{U}}$ (22): the system (18) shows that no spatial derivatives are applied on the memory variables, and hence the numerical integration of (29) does not involve values of the memory variables at other nodes.

At the *irregular points* where the stencil crosses the interface, the smoothness requirement is no longer satisfied. To maintain the accuracy at these

points, an immersed interface method is implemented [27, 22, 23]. Let us take an irregular point $(x_i,\, y_j) \in \Omega_0$. The numerical computation of $\mathbf{U}_{i,j}^{n+1/2}$ requires to use a value at $(x_I,\, y_J) \in \Omega_1$ (figure 3). Instead of using naively the numerical value $\overline{\mathbf{U}}_{I,J}^{n}$, a *modified value* $\mathbf{U}_{I,J}^{*}$ is injected into the scheme, corresponding to a smooth extension of the velocity and stress components on Ω_0 into Ω_1.

Before describing the four steps involved in building $\mathbf{U}_{I,J}^{*}$, it is recalled that during the propagative part (29), the viscoelastic medium behaves like an elastic medium with unrelaxed parameters. The forthcoming derivation is therefore in line with the algorithm developed for elastic media [22], with appropriate physical parameters.

Step 1: high-order interface conditions. First, we seek the interface conditions satisfied by the spatial derivatives of the velocity and stress components at P. For this purpose, the zero-th order interface conditions (26) are differentiated in terms of t. The time derivatives are replaced by spatial derivatives, using the propagative part (29). For instance, the boundary condition $\mathbf{L}_0^0\,\mathbf{U}_0^0 = \mathbf{0}$ results in

$$\frac{\partial}{\partial\, t}\left(\mathbf{L}_0^0\,\mathbf{U}_0^0\right) = -\mathbf{L}_0^0\,\overline{\mathbf{A}}_0\,\frac{\partial}{\partial\, x}\,\mathbf{U}_0^0 - \mathbf{L}_0^0\,\overline{\mathbf{B}}_0\,\frac{\partial}{\partial\, y}\,\mathbf{U}_0^0 = \mathbf{0}. \tag{32}$$

Equations (26) are also differentiated in terms of τ, using the chain-rule. For instance, the boundary condition $\mathbf{L}_0^0\,\mathbf{U}_0^0 = \mathbf{0}$ results in

$$\frac{d}{d\,\tau}\left(\mathbf{L}_0^0\,\mathbf{U}_0^0\right) = \left(\frac{d}{d\,\tau}\,\mathbf{L}_0^0\right)\,\mathbf{U}_0^0 + \mathbf{L}_0^0\left(x^{'}\,\frac{\partial}{\partial\, x}\,\mathbf{U}_0^0 + y^{'}\,\frac{\partial}{\partial\, y}\,\mathbf{U}_0^0\right) = \mathbf{0}. \tag{33}$$

From (32) and (33), a matrix $\mathbf{L}_0^1$ is built such that $\mathbf{L}_0^1\,\mathbf{U}_0^1 = \mathbf{0}$. This matrix depends on τ and on the physical parameters on Ω_0. Applying a similar procedure to the three equations in (26) gives a set of first-order interface conditions. By iterating this process k times, we obtain the k-th order interface conditions

$$\mathbf{C}_1^k\,\mathbf{U}_1^k = \mathbf{C}_0^k\,\mathbf{U}_0^k, \qquad \mathbf{L}_m^k\,\mathbf{U}_m^k = \mathbf{0}, \qquad m = 0, 1. \tag{34}$$

When $k \geq 2$, building the matrices $\mathbf{C}_m^k$ and $\mathbf{L}_m^k$ is a tedious task, which can be greatly simplified by using computer algebra tools. Note lastly that $\mathbf{C}_m^k$ and $\mathbf{L}_m^k$ involve the spatial derivatives $\frac{d^\alpha\, x}{d\,\tau^\alpha}$ and $\frac{d^\alpha\, y}{d\,\tau^\alpha}$ $(\alpha = 1, ...,\, k+1)$, which

provides insights about the local geometry of Γ at P.

Step 2: high-order Beltrami equations. In (29), the viscoelastic medium consists of an elastic medium with unrelaxed parameters, where compatibility conditions are satisfied between some spatial derivatives of the strain components [25]. When expressed in terms of σ, these conditions lead to the Beltrami equation

$$\frac{\partial^2}{\partial x\,\partial y}\,\sigma_{12} = \alpha_2\,\frac{\partial^2}{\partial x^2}\,\sigma_{11} + \alpha_1\,\frac{\partial^2}{\partial x^2}\,\sigma_{22} + \alpha_1\,\frac{\partial^2}{\partial y^2}\,\sigma_{11} + \alpha_2\,\frac{\partial^2}{\partial y^2}\,\sigma_{22}, \tag{35}$$

where

$$\begin{aligned} \alpha_1 &= \frac{\pi_u}{4\,(\pi_u - \mu_u)} = \frac{c_{p_\infty}^2}{4\,\left(c_{p_\infty}^2 - c_{s_\infty}^2\right)}, \\ \alpha_2 &= -\frac{\pi_u - 2\,\mu_u}{4\,(\pi_u - \mu_u)} = \frac{2\,c_{s_\infty}^2 - c_{p_\infty}^2}{4\,\left(c_{p_\infty}^2 - c_{s_\infty}^2\right)}. \end{aligned} \tag{36}$$

The equation (35) is satisfied anywhere in Ω_0. Under suitable smoothness requirements, it can be differentiated as many times as necessary, with respect to x and y. Since the equations thus obtained are also valid along Γ, they can be used to obtain a minimum number of independent components $\mathbf{V}_m^k$

$$\mathbf{U}_m^k = \mathbf{G}_m^k\,\mathbf{V}_m^k, \qquad m = 0,\,1. \tag{37}$$

The algorithm for building the matrices $\mathbf{G}_m^k$ presented in [23] can be easily adapted to (35)-(36). If Ω_1 is not a viscoelastic medium, then (37) is still valid if appropriate Beltrami-like equations are used: see [22] for the fluid-elastic case.

Step 3: high-order boundary values. The high-order boundary conditions in (34) and the high-order Beltrami equations (37) give the underdetermined linear systems

$$\mathbf{L}_m^k\,\mathbf{G}_m^k\,\mathbf{V}_m^k = \mathbf{0}, \quad m = 0,\,1. \tag{38}$$

We obtain

$$\mathbf{V}_m^k = \mathbf{K}_m^k\,\mathbf{W}_m^k, \quad m = 0,\,1, \tag{39}$$

where $\mathbf{K}_m^k$ are the matrices built from the kernel of $\mathbf{L}_m^k\,\mathbf{G}_m^k$. The solution $\mathbf{W}_m^k$ is the minimum set of independent components of the trace of $\mathbf{U}$ and

its spatial derivatives up to the k-th order, on the side Ω_m. Injecting (39) into the high-order jump conditions (34) gives

$$\mathbf{S}_1^k \, \mathbf{W}_1^k = \mathbf{S}_0^k \, \mathbf{W}_0^k, \tag{40}$$

where $\mathbf{S}_m^k = \mathbf{C}_m^k \, \mathbf{G}_m^k \, \mathbf{K}_m^k$. The underdetermined system (40) is solved

$$\mathbf{W}_1^k = \left(\left(\mathbf{S}_1^k\right)^{-1} \mid \mathbf{R}_{\mathbf{S}_1^k} \right) \begin{pmatrix} \mathbf{W}_0^k \\ \\ \mathbf{\Lambda}^k \end{pmatrix}, \tag{41}$$

where $(\mathbf{S}_1^k)^{-1}$ is the least-squares pseudo-inverse of $\mathbf{S}_1^k$, $\mathbf{R}_{\mathbf{S}_1^k}$ is the matrix containing the kernel of $\mathbf{S}_1^k$, and $\mathbf{\Lambda}^k$ is a set of Lagrange multipliers. To build $(\mathbf{S}_1^k)^{-1}$ and $\mathbf{R}_{\mathbf{S}_1^k}$, a singular value decomposition of $\mathbf{S}_1^k$ is performed.

Step 4: construction of modified values. Let P be the orthogonal projection of $(x_I, \, y_J)$ on Γ (figure 3). The coefficients of 2-D Taylor expansions around P are put in the matrix $\mathbf{\Pi}_{i,j}^k$:

$$\mathbf{\Pi}_{i,j}^k = \left(\mathbf{I}_5, ..., \frac{1}{\beta \, ! \, (\alpha - \beta) \, !} \, (x_i - x_P)^{\alpha - \beta} (y_j - y_P)^{\beta} \, \overline{\mathbf{I}}_5, ..., \frac{(y_j - y_P)^k}{k \, !} \, \overline{\mathbf{I}}_5 \right), \tag{42}$$

where $\mathbf{I}_5$ is the 5×5 identity matrix, $\alpha = 0, ..., k$ and $\beta = 0, ..., \alpha$. The modified value at $(x_I, \, y_J)$ is

$$\mathbf{U}_{I,J}^* = \mathbf{\Pi}_{I,J}^k \, \mathbf{U}_0^k. \tag{43}$$

The trace $\mathbf{U}_0^k$ in (43) still remains to be determined in terms of the interface conditions and the numerical values at surrounding nodes. For this purpose, let us take the disc $\mathcal{D}$ centered at P with radius q. At the grid nodes of $\mathcal{D} \cap \Omega_0$, k-th order Taylor expansion of the solution at P, and the conditions (37) and (39), give

$$\begin{aligned} \overline{\mathbf{U}}(x_i, y_j, t_n) &= \mathbf{\Pi}_{i,j}^k \, \mathbf{U}_0^k + \mathcal{O}(\Delta \, x^{k+1}), \\ &= \mathbf{\Pi}_{i,j}^k \, \mathbf{G}_0^k \, \mathbf{K}_0^k \, \mathbf{W}_0^k + \mathcal{O}(\Delta \, x^{k+1}), \\ &= \mathbf{\Pi}_{i,j}^k \, \mathbf{G}_0^k \, \mathbf{K}_0^k \, (\mathbf{1} \mid \mathbf{0}) \begin{pmatrix} \mathbf{W}_0^k \\ \\ \mathbf{\Lambda}^k \end{pmatrix} + \mathcal{O}(\Delta \, x^{k+1}). \end{aligned} \tag{44}$$

At the grid nodes of $\mathcal{D} \cap \Omega_1$, k-th order Taylor expansion of the solution at P, and the interface conditions (37), (39) and (41), give

$$\begin{aligned}
\overline{\mathbf{U}}(x_i, y_j, t_n) &= \mathbf{\Pi}^k_{i,j}\, \mathbf{U}^k_1 + \mathcal{O}(\Delta\, x^{k+1}), \\
&= \mathbf{\Pi}^k_{i,j}\, \mathbf{G}^k_1\, \mathbf{K}^k_1\, \mathbf{W}^k_1 + \mathcal{O}(\Delta\, x^{k+1}), \\
&= \mathbf{\Pi}^k_{i,j}\, \mathbf{G}^k_1\, \mathbf{K}^k_1 \left(\left(\mathbf{S}^k_1\right)^{-1} \mid \mathbf{R}_{\mathbf{S}^k_1} \right) \begin{pmatrix} \mathbf{W}^k_0 \\ \\ \mathbf{\Lambda}^k \end{pmatrix} + \mathcal{O}(\Delta\, x^{k+1}).
\end{aligned} \tag{45}$$

The equations (44) and (45) are written using an adequate matrix $\mathbf{M}$

$$\left(\overline{\mathbf{U}}(.,\, t_n)\right)_{\mathcal{D}} = \mathbf{M} \begin{pmatrix} \mathbf{W}^k_0 \\ \\ \mathbf{\Lambda}^k \end{pmatrix} + \begin{pmatrix} \mathcal{O}(\Delta\, x^{k+1}) \\ \vdots \\ \mathcal{O}(\Delta\, x^{k+1}) \end{pmatrix}. \tag{46}$$

The radius q is chosen so that (46) is overdetermined. The exact values are then replaced by numerical ones and the Taylor rests are removed. The least-squares inverse of the matrix $\mathbf{M}$ is denoted by $\mathbf{M}^{-1}$. Since the Lagrange multipliers $\mathbf{\Lambda}^k$ are not involved in (43), $\mathbf{M}^{-1}$ is restricted to $\overline{\mathbf{M}}^{-1}$, so that

$$\mathbf{W}^k_0 = \overline{\mathbf{M}}^{-1}\, \left(\overline{\mathbf{U}}^n\right)_{\mathcal{D}}. \tag{47}$$

The modified value follows from (37), (39), (43) and (47):

$$\mathbf{U}^*_{I,J} = \mathbf{\Pi}^k_{I,J}\, \mathbf{G}^k_0\, \mathbf{K}^k_0\, \overline{\mathbf{M}}^{-1}\, \left(\overline{\mathbf{U}}^n\right)_{\mathcal{D}}. \tag{48}$$

A similar algorithm is applied at each irregular point along Γ. Since the matrices in (48) do not depend on t, they are computed in a preprocessing step and stored. At each time step, only the matrix-vector products in (48) are performed at each irregular point before being injected into the scheme. The matrices involved here are small, amounting typically to 5×100. After optimizing the computer codes, the additional cost due to the use of the immersed interface method becomes negligible, i.e. it accounts for less than 1% of the total computational time. Lastly, k still remains to be defined. Theoretically, $k = r$ is necessary to ensure local r-th order accuracy of the scheme. However, $k = r - 1$ suffices to keep the global error to the r-th order [15].

5. Numerical experiments

5.1. Configuration

Here we focus on viscoelastic / fluid configurations. The physical parameters in the viscoelastic medium Ω_0 are:

$$\rho = 1200 \ \text{kg/m}^3,\ c_{p_0} = 2800 \ \text{m/s},\ c_{s_0} = 1400 \ \text{m/s},\ Q^p_{ref} = 20,\ Q^s_{ref} = 15,$$

with $N = 3$ relaxation mechanisms, and in the fluid medium Ω_1 they are:

$$\rho = 1000 \ \text{kg/m}^3,\ c = 1500 \ \text{m/s}.$$

The source is an homogeneous plane wave, the time evolution of which is given by a combination of truncated sinusoids

$$h(t) = \begin{cases} \displaystyle\sum_{m=1}^{4} a_m \, \sin(\beta_m \, \omega_c \, t) & \text{if } \ 0 < t < \dfrac{1}{f_c}, \\ \\ 0 \ \text{otherwise}, \end{cases} \tag{49}$$

where $\beta_m = 2^{m-1}$, $\omega_c = 2\pi \, f_c$; the coefficients a_m are: $a_1 = 1$, $a_2 = -21/32$, $a_3 = 63/768$, $a_4 = -1/512$. The signal thus obtained is C^6 and has a central frequency $f_c = 30$ Hz. After optimizing κ_ℓ between $f_0 = f_c/10$ and $f_1 = 10 \, f_c$ (7), then equation (11) is used to obtain the high-frequency limits $c_{p_\infty} = 3161$ m/s and $c_{s_\infty} = 1645$ m/s.

The discretization mesh is $\Delta x = \Delta y = 1$ m. The time step follows from $c_{p_\infty} \, \Delta t / \Delta x = 0.85$. On the plates, σ_{11} is shown with a green-red palette in the case of P waves and a yellow-magenta palette in that of S waves. The distinction between these waves is based on numerical estimates of div $\mathbf{v}$ and curl $\mathbf{v}$. Lastly, the position of a slice is denoted on the plates by horizontal segments.

5.2. Plane interface

The first test is conducted on a plane interface between the fluid and the viscoelastic medium. The angle between the straight line and the horizontal axis is equal to 70 degrees. A homogeneous acoustic plane wave (IP), having a wave vector inclined at an angle of 10 degrees, propagates in the fluid and interacts with the interface. The reflected acoustic wave (RP) and the viscoelastic transmitted compressional (TP) and shear (TS) waves are

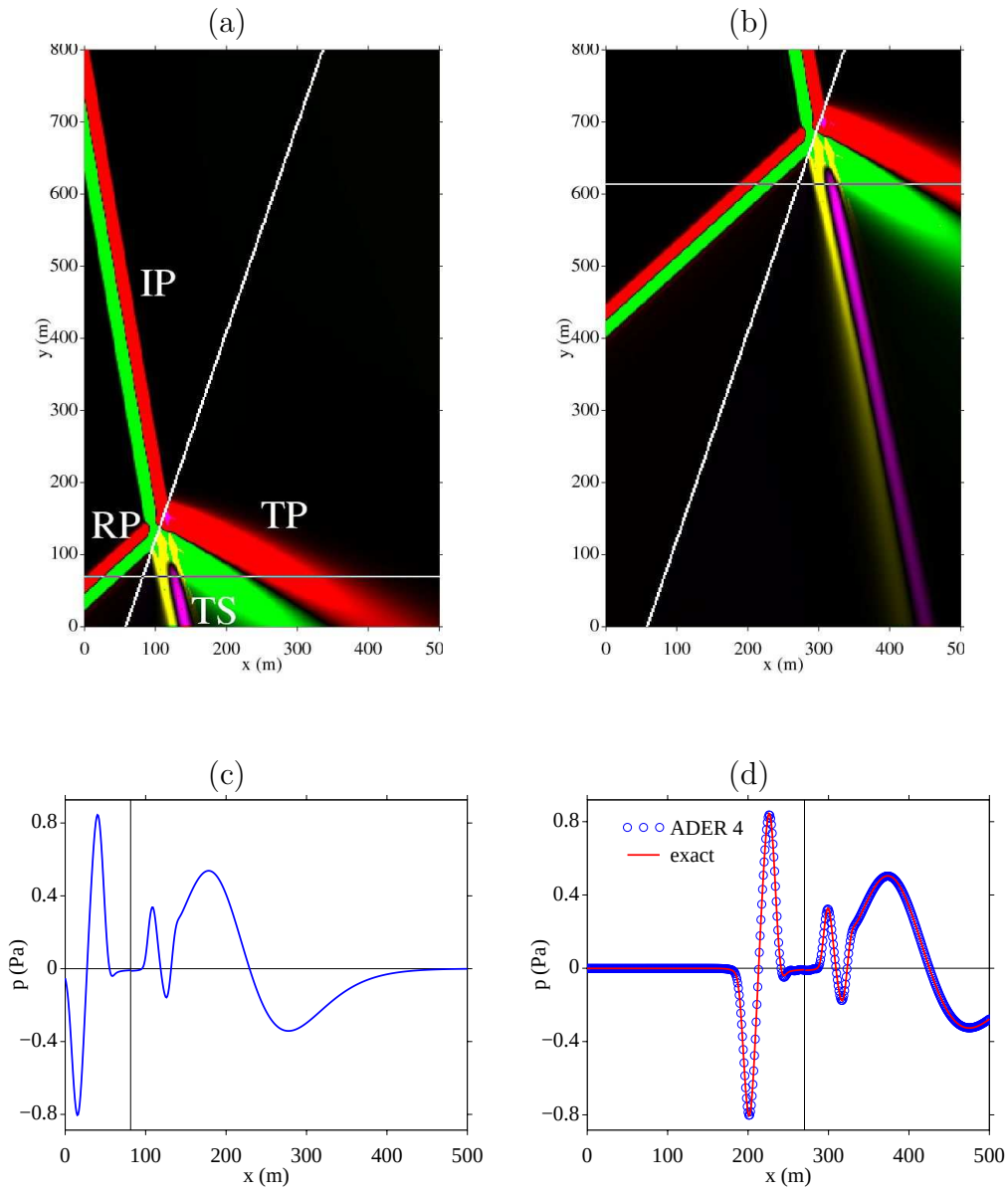

Figure 4: Plane interface between a fluid (on the left) and a viscoelastic medium (on the right). Initial instant (a-c) and after 700 time steps (b-d). IP: incident homogeneous acoustic wave; RP: reflected inhomogeneous acoustic wave; TP, TS: transmitted inhomogeneous compressional and shear viscoelastic waves.

inhomogeneous: their wave vector forms a non-null angle with the direction where they are attenuated. See [20, 10, 11, 5, 6, 30] for further details on this topic. Figure 4 shows the incident field (a-c) and after 700 integration time steps (b-d), which corresponds to roughly 6 propagation wavelengths. Excellent agreement is observed between the numerical and exact values.

5.3. Circular interface

The immersed interface method depends on the curvature of the interface and its successive derivatives [22, 23]. To test the method with a non-null curvature, we now examine a circular interface with a radius of 60 m. The fluid and the viscoelastic medium are outside and inside the circle, respectively. The incident field is a plane acoustic wave with a horizontal wave vector. Figure 5 shows the field at the initial instant (a-b), after 220 time steps (c-d) and after 440 time steps (e-f). Classical conversions and scattering phenomena are observed. Excellent agreement is found to exist with the analytical solutions. The latter are computed using Fourier techniques and decomposing the plane waves on the basis of Bessel functions.

5.4. Multiple scattering in random medium

In the previous tests, the validity of the numerical scheme and the immersed interface method was confirmed in the case of academic configurations. We now take a complex medium composed of 60 viscoelastic cylinders randomly embedded in water. The computations are performed on 2000×3000 grid nodes. Figure 6 shows the initial field (a) and the scattered fields after 2200 time steps (b), when the incident wave has propagated over a distance corresponding to 12 wavelengths.

6. Perspectives

The propagation of mechanical waves in dissipative solids was addressed numerically in the time domain. To avoid having to deal with convolution products, memory variables were introduced. Evolution equations were splitted into two parts: the propagative part was solved numerically using a fourth-order scheme for hyperbolic systems; and the diffusive part was solved exactly. The jump conditions were discretized by means of an immersed interface method, which introduced a subcell resolution on a Cartesian grid.

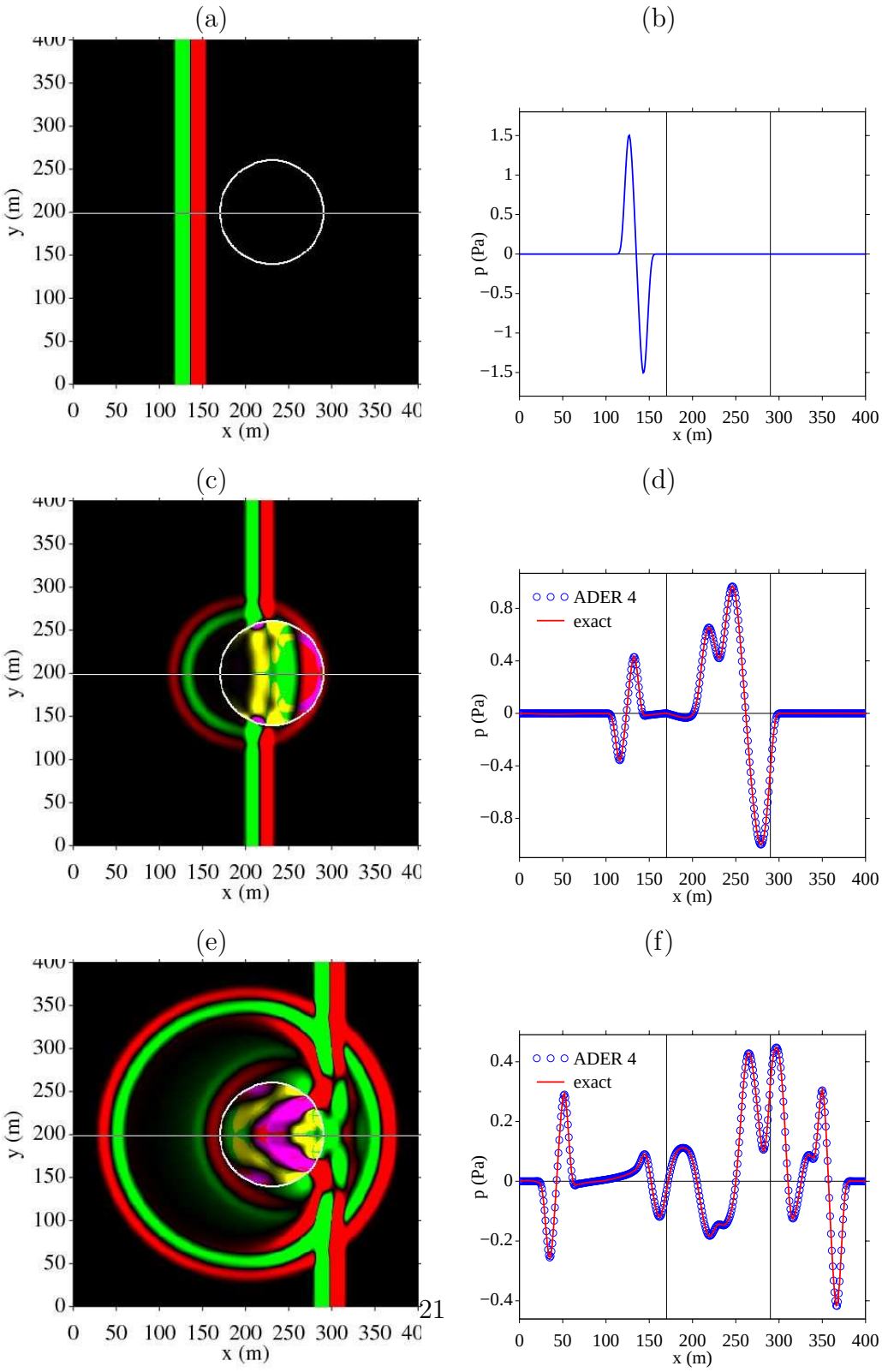

Figure 5: Circular interface between a fluid (outside) and a viscoelastic medium (inside). Initial field (a-b), after 220 time steps (c-d) and 440 time steps (e-f).

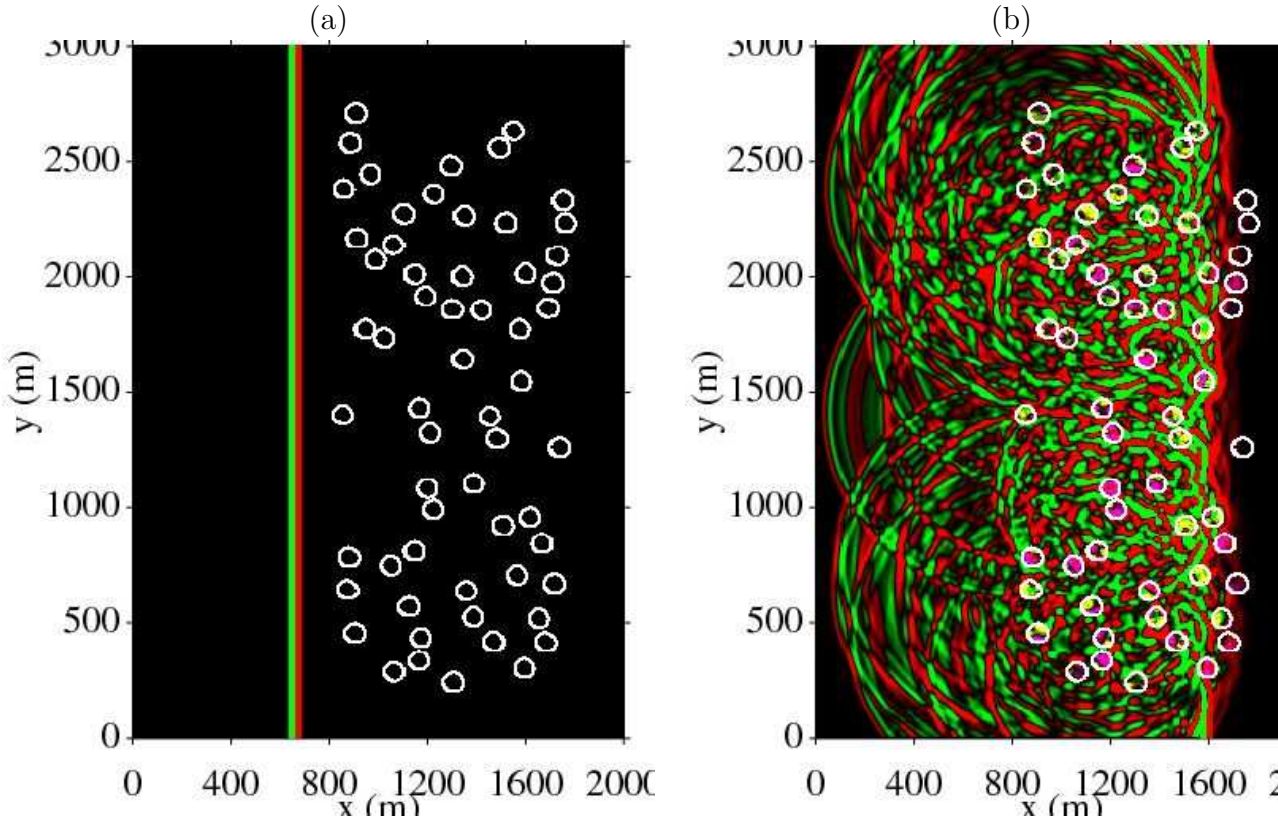

Figure 6: Initial (a) and scattered field after 2200 time steps (b).

The numerical methods presented here make it possible to simulate physically relevant numerical experiments, for instance multiple scattering in random media as performed in section 5.4. By applying signal processing tools on the simulated data, it is possible to determine the properties of the *effective medium* which is equivalent to the disordered medium investigated [9]. This numerical approach can be used advantageously instead of the methods usually adopted by physicists so far: real experiments are expensive, and analytical methods can be used only with very small concentrations of scatterers. The latter limitation is particularly penalizing in the case of concrete, where the concentration of aggregates lies typically around 40%.

[1] K. Aki, P. G. Richards, *Quantitative Seismology. Theory and Methods. Vol. 1*, Freeman, New-York, 1980.

[2] S. Asvadurov, L. Knizhnerman, J. Pabon, *Finite-difference modeling of viscoelastic materials with quality factors of arbitrary magnitude*, Geophysics, 69-3 (2004), pp. 817–824.

[3] E. Bécache, A. Ezziani, P. Joly, *A mixed finite element approach for viscoelastic wave propagation*, Computational Geosciences, 8 (2004), pp. 255-299.

[4] J. O. Blanch, J. O. A. Robertsson, W. W. Symes, *Modeling of a constant Q: methodology and algorithm for an efficient and optimally inexpensive viscoelastic technique*, Geophysics, 60-1 (1995), pp. 176–184.

[5] R. D. Borcherdt, *Reflection and refraction of type-II S waves in elastic and anelastic media*, Bull. Seism. Soc. Am., 67-1 (1977), pp. 43–67.

[6] R. D. Borcherdt, *Reflection-refraction of general P- and type-I S waves in elastic and anelastic solids*, Geophys. J. R. astr. Soc., 70 (1982), pp. 621–638.

[7] J. M. Carcione, *Seismic modeling in viscoelastic media*, Geophysics, 58-1 (1993), pp. 110–120.

[8] J. M. Carcione, *Wave Fields in Real Media: Wave Propagation in Anisotropic, Anelastic, Porous and Electromagnetic Media*, Pergamon, 2007.

[9] M. Chekroun, L. le Marrec, B. Lombard, J. Piraux, O. Abraham, *Comparisons between multiple scattering methods and direct numerical simulations for elastic wave propagation in concrete*, Springer Proceedings in Physics, 128 (2009), pp. 317–327.

[10] H. F. Cooper, E. L. Reiss, *Reflection of plane viscoelastic waves from plane boundaries*, J. Acoust. Soc. Am., 39-6 (1966), pp. 1133–1138.

[11] H. F. Cooper, *Reflection and transmission of oblique plane waves at a plane interface between viscoelastic media*, J. Acoust. Soc. Am., 42-5 (1967), pp. 1064–1069.

[12] S. M. Day, J. B. Minster, *Numerical simulation of attenuated wavefields using a Padé approximant method*, Geophys. J. R. astr. Soc., 78 (1984), pp. 105–118.

[13] H. Emmerich, M. Korn, *Incorporation of attenuation into time-domain computations of seismic wave fields*, Geophysics, 52-9 (1987), pp. 1252–1264.

[14] J. P. Groby, C. Tsogka, *A time domain method for modeling viscoacoustic wave propagation*, J. Comput. Acoust., 14-2 (2006), pp. 201–236.

[15] B. Gustafsson, *The convergence rate for difference approximations to mixed initial boundary value problems*, Math. Comput., 29-130 (1975), pp. 396-406.

[16] D. Komatitsch, J. Tromp, *Introduction to the spectral-element method for 3-D seismic wave propagation*, Geophys. J. Int., 139 (1999), pp. 806-822.

[17] E. Kjartansson, *Attenuation of seismic waves in rocks and applications in energy exploration*, PhD thesis, Stanford University, 1979.

[18] R. J. LeVeque, *Finite Volume Methods for Hyperbolic Problems*, Cambridge University Press, 2002.

[19] Z. Li, K. Ito, *The Immersed Interface Method: Numerical Solutions of PDEs Involving Interfaces and Irregular Domains*, SIAM Frontiers in Applied mathematics, 33, 2006.

[20] F. J. Lockett, *The reflection and refraction of waves at an interface between viscoelastic materials*, J. Mech. Phys. Solids, 10 (1962), pp. 53–64.

[21] B. Lombard, *Modélisation Numérique de la Propagation et de la Diffraction d'Ondes Mécaniques*, HDR thesis, Aix-Marseille 2 (2010), `http://tel.archives-ouvertes.fr/docs/00/44/88/97/PDF/Hdr.pdf`.

[22] B. Lombard and J. Piraux, *Numerical treatment of two-dimensional interfaces for acoustic and elastic waves*, J. Comput. Phys., 195-1 (2004), pp. 90–116.

[23] B. Lombard, J. Piraux, *Numerical modeling of elastic waves across imperfect contacts*, SIAM J. Scient. Comput., 28-1 (2006), pp. 172–205.

[24] F. Lörcher, C. Munz, *Lax-Wendroff-type schemes of arbitrary order in several space dimensions*, IMA J. Numer. Anal., (2005), pp. 1-28.

[25] A. E. H. Love, *A Treatise on the Mathematical Theory of Elasticity*, New-York Dover Publications, 1944.

[26] P. Moczo and J. Kristek, *On the rheological models used for time-domain methods of seismic wave propagation*, Geophys. Res. Lett., 32 (2005), L01306.

[27] J. Piraux, B. Lombard, *A new interface method for hyperbolic problems with discontinuous coefficients: 1D acoustic example*, J. Comput. Phys., 168-1 (2001), pp. 227–248.

[28] J. O. A. Robertsson, J. O. Blanch, W. W. Symes, *Viscoelastic finite-difference modeling*, Geophysics, 59-9 (1994), pp. 1444–1456.

[29] T. Schwartzkopff, M. Dumbser, C. Munz, *Fast high order ADER schemes for linear hyperbolic equations*, J. Comput. Phys., 197-2 (2004), pp. 532–539.

[30] L. Wennerberg, *Snell's law for viscoelastic materials*, Geophys. J. R. astr. Soc., 81 (1985), pp. 13–18.

[31] T. Xu, G. A. McMechan, *Composite memory variables for viscoelastic synthetic seismograms*, Geophys. J. Int., 121 (1995), pp. 634–639.